Applied Catalysis B: Environmental 343 (2024) 123551

Contents lists available at ScienceDirect

Applied Catalysis B: Environmental

journal homepage: www.elsevier.com/locate/apcatb

# Enhancing CO diffusion for selective acetate production via CO reduction on copper catalyst

Junmei Chen [a], Lei Chen [a], Jingyi Chen [a], Di Wang [a], Yilin Zhao [a], Lan Wen [a], Shibo Xi [b], Lei Wang [a,c,*]

[a] Department of Chemical and Biomolecular Engineering, National University of Singapore, Engineering Drive 4, Singapore 117585, Singapore
[b] The Institute of Sustainability for Chemicals, Energy and Environment, A*STAR, 1 Pesek Road Jurong Island, Singapore 627833, Singapore
[c] Centre for Hydrogen Innovations, National University of Singapore, 1 Engineering Drive 3, Singapore

ARTICLE INFO

*Keywords:*
Electrocatalytic CO reduction
Polymer Coating
Gas diffusion
Acetate

ABSTRACT

The productivity of multi-carbon products in electrocatalytic CO reduction is greatly influenced by the local concentration of CO. Herein, we present a facile strategy for modulating the local concentration of CO under atmospheric pressure via polymer coating, which enables selective, active and stable production of acetate on a Cu model-catalyst. Specifically, we coat the Cu-catalyst with a fluorinated polymer, forming an optimized gas-involving reaction interface. This approach enhances the CO diffusion to catalyst surfaces and increases the hydrophobicity of the catalyst layer, resulting in enhanced acetate selectivity of over 50% with a high partial current density of $-0.65$ A $cm^{-2}$ on Cu-catalyst. This represents an over 3 folders of enhancement compared to the pristine Cu-catalyst. Furthermore, this optimized reaction interface led to a stable COR electrolysis over a duration of 70 h. Our strategy offers valuable insights for designing efficient catalytic interface in various electrochemical reactions that involve gas diffusion.

## 1. Introduction

Electrochemical $CO_2$ reduction ($CO_2R$) is recognized as one of the promising technologies to mitigate the greenhouse effect by converting $CO_2$ into valuable chemicals and fuels, particularly when coupled with renewable electricity sources, *i. e.*, wind, tide, and solar, *etc*. [1–4] Alkaline electrolytes are widely used in $CO_2R$ as they tend to enhance the overall energy efficiency by reducing the overpotential and improving the selectivity towards multi-carbon products [5–7]. However, direct $CO_2R$ in alkaline electrolyte suffers from severe carbonate formation, resulting in substantially decreased carbon utilization efficiency, system stability, and large energy penalty associated with the $CO_2$ regeneration from carbonate [8–11]. In contrast, conducting CO reduction (COR) can effectively address the above challenges owning to the chemical stability of CO in alkaline solutions [12–16].

Reaction microenvironment, including factors such as local $CO_2$/CO concentration [17,18], pH [19,20], electric field [21,22], cation effect [23,24] and the electrode hydrophobicity [25,26], plays significant role in determining the activity and products selectivity of $CO_2R$/COR. For instance, the CO partial pressure ($P_{CO}$) has been found to influence both the COR activity and selectivity by modulating the surface coverage of CO according to henry's law [27]. Specifically, at relatively negative potentials, the COR activity increased with $P_{CO}$ until the Cu-based catalyst surface is fully covered by CO. Particularly, the selectivity towards acetate, a valuable chemical product, has been observed to increase with increasing $P_{CO}$ [28]. However, this high selectivity of acetate is achieved on the expense of applying significantly high pressure of CO, which can introduce additional setup and cost for the future implementation of COR. Therefore, there is a need to develop strategies that promote the activity/selectivity of COR towards acetate under mild conditions, such as at low or ambient pressures.

In this work, we present a facile strategy for enhancing the selectivity of acetate formation from COR by promoting the local CO diffusion through polymer coating on the catalyst surface, as illustrated in Fig. 1. Specifically, a hydrophobic polymer was uniformly coated onto Cu catalyst, forming a thin layer on the catalyst surface. Two factors are taken into consideration to select the appropriate polymer. First, the polymer should possess high gas (*i.e.*, CO) permeability to facilitate

* Corresponding author at: Department of Chemical and Biomolecular Engineering, National University of Singapore, Engineering Drive 4, Singapore 117585, Singapore.
*E-mail address:* wanglei8@nus.edu.sg (L. Wang).

https://doi.org/10.1016/j.apcatb.2023.123551
Received 23 June 2023; Received in revised form 5 October 2023; Accepted 20 November 2023
Available online 22 November 2023

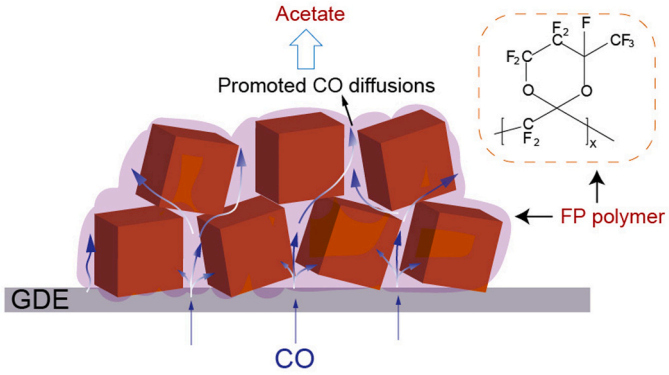


**Fig. 1.** Illustration of the proposed strategy for promoting the local CO diffusion via polymer coating. Red cube: catalyst; purple shade: polymer coatings.

efficient CO diffusion across the catalyst surface. Second, it should exhibit stable hydrophobic properties to maintain its integrity of gas diffusion channels during COR. Based upon these considerations, we employed a fully fluorinated polymer (FP, commercial name: PT95, see details in Experimental Section) and used the cubic $Cu_2O$ as the model catalyst to construct the polymer/catalyst composite (FP/$Cu_2O$) as shown in Fig. 1. After application of polymer coating, the FP/$Cu_2O$ exhibited a substantially enhanced acetate selectivity of 50.2% with a high acetate partial current density of −0.65 A $cm^{-2}$. In comparison, the pristine $Cu_2O$ electrode achieved acetate selectivity of only 19% with partial current density of −0.19 A $cm^{-2}$, under the same conditions. Comprehensive physical characterizations and mechanistic investigations suggest that the improved acetate selectivity and activity are due to the enhanced local $P_{CO}$ induced by the gas diffusion channel within the polymer layer, rather than changes in the morphology, crystal structure, or chemical states of $Cu_2O$ during COR. This facile yet effective strategy offers a promising approach for further enhancing acetate formation when combined with other effective catalysts.

## 2. Experimental section

### 2.1. Chemicals

Ultrapure Millipore water (18.2 MΩ cm) was used throughout the experiments. Potassium hydroxide (99.99%), potassium sulfate (90%), Nafion™ 117 solution (5% in a mixture of lower aliphatic alcohols and water), PTFE solution (60% dispersion in $H_2O$), Ethanol (ACS reagent) were purchased from Sigma-Aldrich. Fully perfluorinated polymer (FP) and Fluorinert electronic liquid (FC-770) were purchased from Shanghai BiChen industrial Co., LTD. The Nafion 117 membrane was purchased from Fuel Cell Store. All chemicals were used without further purification. The carbon paper used for flow cell (YLS-30 T) was purchased from Suzhou Sinero Technology CO., LTD and the carbon paper (P75T) used for H-cell was purchased from fuel cell store.

### 2.2. Synthesis of $Cu_2O$ cube

The method for synthesizing Copper oxide cubes was modified based on a previously reported method [29]. In a typical procedure, 1 mL of 1.2 M $CuSO_4.5\ H_2O$ solution was rapidly injected into 400 mL deionized water and vigorously stirred for 5 min. Then, 1 mL of 4.8 M NaOH solution was injected into the solution. The previously clear blue solution immediately turned turbid blue, indicating the precipitation of $Cu(OH)_2$. After another 5 min of stirring, 1 mL of 1.2 M ascorbic acid was injected as a reducer and the solution was stirred for another 30 min. The colour of the solution rapidly changed from turbid blue to yellowish brown. Finally, the product was washed twice with ethanol and water, and free-dried overnight for further use.

### 2.3. Material characterization

FESEM images were taken from a scanning electron microscope (JEOL, JSM-7610 F field). Prior to the SEM test, we applied Pt sputtering onto the surface of $Cu_2O$ cubes for 90 s at a current of 30 mA to enhance the conductivity of the sample. Combined field-emission transmission electron microscopy (FETEM, JEOL JEM-2100, operated at 200 kV) was applied to probe the nano-scale morphology. X-ray photoelectron spectroscopy measurements were performed on a Kratos AXIS Ultra spectrometry equipped with a monochromatized Al Kα X-ray source and a concentric hemispherical analyzer. The X-ray diffraction data were collected on Shimadzu XRD-6000 X-ray diffractometer with a Cu Kα as X-ray source at a scan rate of 5° $min^{-1}$. In-situ XAS experiments were performed at XAFCA beamline of Singapore Synchrotron Light Source under fluorescence mode. Cu K-edge XANES spectra were collected. Athena was used for data processing. $CO_2$ adosprtion isotherms was conducted on Micromeritics ASAP 2020 analyzer (3Flex Version 5.02) under room temperature. Specifically, for $CO_2$ adsorption isotherm experiment, ~100 mg polymer membrane was firstly degassed under a vacuum for 6 hours at 393.15 K to ensure a complete removal of impurities. Upon completion of degassing, the samples were cooled down to room temperature and transferred to the analysis port. To manufacture the polymer membranes, 3 mL of each polymer solution was drop-cast onto a PTFE film, followed by heating to 80 °C. As the solvents gradually evaporated, the polymer membranes were formed. CO permeability test was conducted on a home-made gas permeation apparatus using MKS instrument (Andover, MA, USA), as described previously[30].

### 2.4. Electrode preparation

A 1% full fluorinated polymer (FP) solution was prepared by dispersing FP powder into electronic liquid. Catalyst inks were prepared for the polymer/$Cu_2O$ electrodes as follows: 15 mg of $Cu_2O$ cubes were dispersed into 1 mL of fluorinert electronic liquid, and specific amounts (5 μL, 20 μL, 60 μL) of the 1 wt% FP solution were added. As for the comparison sample, 15 mg of $Cu_2O$ was dispersed in 1 mL of a mixture containing 50% ethanol and 50% $H_2O$, followed by the addition of 75 μL of the 5 wt% Nafion solution. The addition of 20 μL FP solution led to the optimal COR performance. These inks were then sonicated for 30 min to form homogeneous solutions. These inks were subsequently sprayed coated onto 2.5 * 4 $cm^2$ carbon fiber papers (YLS-30 T), and vacuum-dried for 5 h at 80 °C to ensure complete evaporation of the solvents. The prepared electrodes were cut into 2.5 * 1 $cm^2$ and used as cathodes in the flow cell. The final catalyst loading was determined through weighting the mass differences of the carbon paper before and after catalyst loading, with the loading calculated to be approximately 1 mg/$cm^2$. To increase the hydrophobicity of carbon paper, it was pre-treated on the back of gas diffusion layer with PTFE solutions. To do so, the 60% PTFE solution was diluted to 10% with water, then 2 mL of this dilute solution was spray-coated onto the carbon paper with an area of 10 $cm^2$. The PTFE treated carbon paper was then calcinated at 330 °C in a muffle furnace for 30 min to remove the surfactant and form a hydrophobic PTFE layer.

For H-cell electrodes, the same catalyst ink preparation process was utilized as described above. The ink was then spray coated onto carbon paper (P75T) with an area of 1 * 2 $cm^2$, where the actual working area (catalyst loading area) is 1 * 1 $cm^2$.

### 2.5. Flow cell assembly

The flow cell was purchased from GaossUnion, as illustrated in Fig. S1. This cell was assembled by stacking a gas chamber, a catalyst-loaded GDE cathode, a catholyte chamber (where a Ag/AgCl reference electrode locates), a proton exchange membrane (Nafion 117), an anolyte chamber and an $IrO_2$-loaded Ti mesh anode in sequence. During

COR measurements, 24 sccm of CO was continuously fed to the cathode gas chamber by a digital mass flow controller (sevenstar, MFC CS200-A), while the electrolytes were circulated through the catholyte and anolyte chambers at 3 mL $min^{-1}$ and 5 mL $min^{-1}$, respectively, with the aid of peristaltic pumps. When it is necessary to collect liquid products for analysis, we quickly transfer the electrolyte inlet into a fresh electrolyte. After the tubes and the flow cell are filled with fresh electrolyte, we extract 1 mL of the electrolyte from the electrolyte outlet for analysis. After electrolyte collection, both inlet and outlet lines are repositioned back to the chamber for electrolyte circulate (Fig. S2). For the CO partial pressure dependent COR experiment, the CO partial pressure was adjusted by mixing CO with $N_2$.

### 2.6. H-cell assembly

H-cell was used in this work to analyze the electrochemical active surface area (ECSA) of the catalysts. This cell was purchased from GaossUnion, consists of airtight two-compartment. In the anodic compartment, a Pt foil with an area of 1 * 2 $cm^2$ was placed. The cathodic compartment housed the reference electrode (Ag/AgCl) and the working electrode. These two compartments were separated by a piece of Nafion 117 membrane, and each compartment contained 20 mL of a 0.5 M $KHCO_3$ electrolyte. Before conducting the ECSA measurements, the electrolyte was purged with 99.999% Ar for 30 min to remove any residual oxygen. The ECSA analysis was performed by scanning at the potential range from −0.22 V to −0.32 V (vs. RHE), at least scan for 10 times at different scan rates.

### 2.7. In-situ $OH^-$ striping experiment

Flow cell was used for this experiment. To conduct the $OH^-$ striping experiment, 1 M KOH was employed as the electrolyte, which flowed to the cathode at a rate of 1 mL $min^{-1}$ without recirculation. In order to prevent structural deterioration of $Cu_2O$ caused by alkaline electrolyte, a

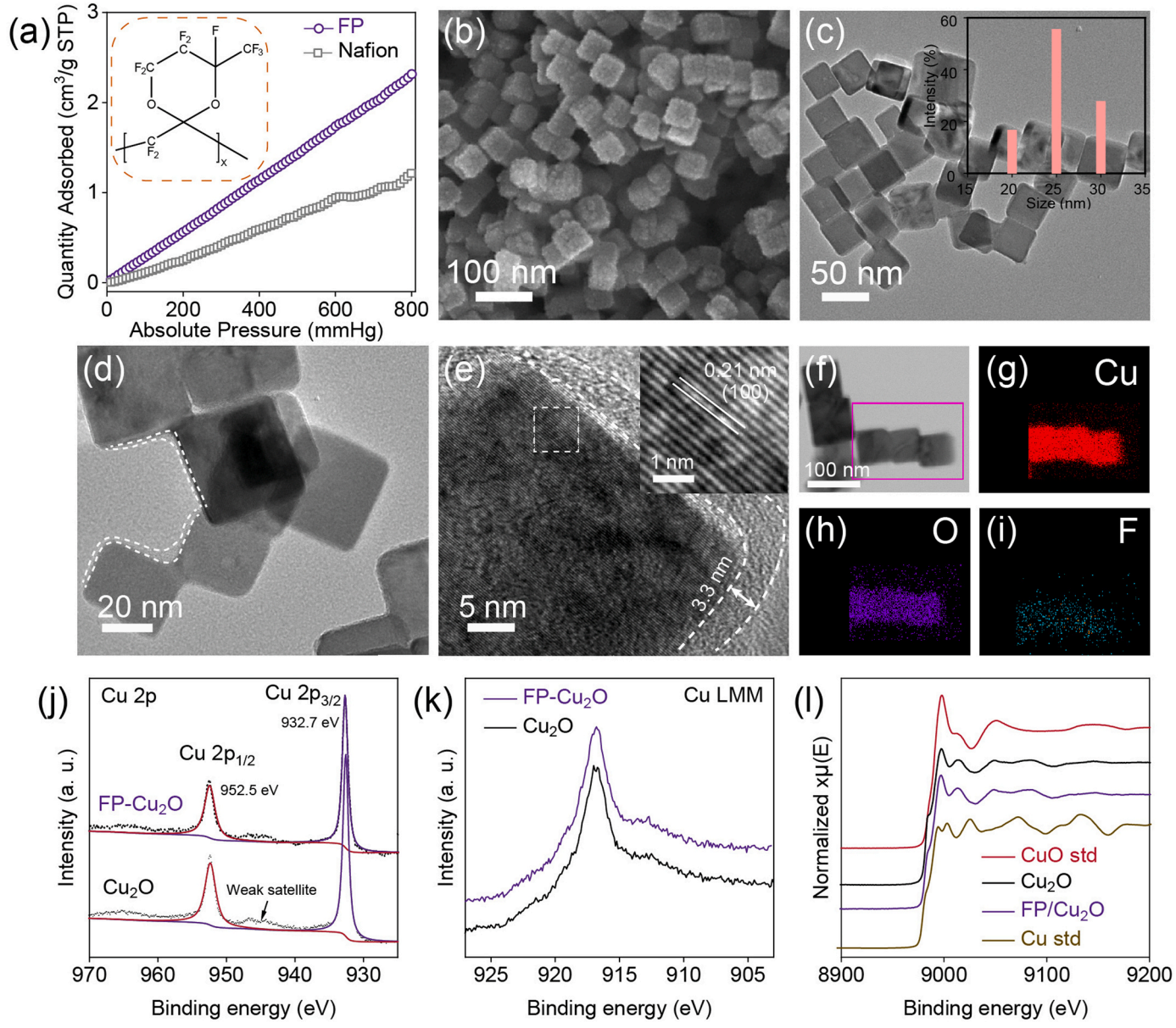


**Fig. 2.** Characterizations of FP, $Cu_2O$ cubes and FP/$Cu_2O$. (a) $CO_2$ adsorption isotherms, insert is the chemical structure of FP; (b) SEM and (c) TEM of synthesized $Cu_2O$ cubes, the insert in Fig. (c) is the size distribution of $Cu_2O$, the samples used for SEM testing were pre-sputtered with a layer of Pt to enhance their conductivity; (d) TEM and (e) HRTEM of FP/$Cu_2O$ (insert is an enlarged inverse FFT view of region in the dash square of (e)); (f-i) EDX element mapping of FP/$Cu_2O$; XPS spectra of (j) Cu *2p*, (k) Cu LMM Auger, and (l) XAS spectra of Cu K-edge.

0.5 M $KHCO_3$ solution was introduced prior to applying the negative potential. Once the reduction process was initiated, the electrolyte was switched to 1 M KOH. $Cu_2O$ was initially reduced at $-0.3$ A $cm^{-2}$ for 2 min using CO gas, followed by an immediate switch to $N_2$ to carry out the $OH^-$ striping process within a potential range of 0.3–0.5 V vs. RHE for 5 cycles. Afterwards, the gas was switched back to CO for another 20 mins reduction, and the aforementioned process was repeated for time-dependent $OH^-$ stripping.

### 2.8. In-situ XAS measurement

In-situ X-ray absorption spectroscopy measurement of catalysts at the Cu K-edges were conducted at the XAFCA beamline of Singapore Synchrotron Light Source using a fluorescence mode. The testing cell used was the same as our flow cell. The in-situ spectra of polymer/Cu catalysts were collected from the backside of the carbon paper electrode. The electrochemical cell was controlled by a CHI760E potentiostat. A double channel Peristaltic pump was used to purge 1 M KOH into both chambers of the flow cell. The samples at the open circuit voltage (OCV) state were measured without electrolyte to prevent structural erosion of $Cu_2O$ caused by the alkaline electrolyte.

## 3. Results and discussion

### 3.1. Preparing the Polymer/Cu composites

We first assessed the gas adsorption capacity of FP (Fig. 2a) by measuring $CO_2$ adsorption isotherms. Due to the institutional safety regulations, we were unable to conduct CO adsorption isotherm measurements. However, considering the similar physical of $CO_2$ and CO, we anticipate that the results obtained are relevant in this study. For comparison, Nafion-based polymer was examined accordingly, as it is widely used as a binder for preparing the catalyst layer of gas diffusion electrodes (GDE) [31]. Note that the $CO_2$ adosrption measurements for the different polymers were conducted using the corresponding polymer membranes (See details in Experimental section). The actual CO adsorption capacity during electrolysis was potentially reduced due to the polymer swelling [32,33]. As shown in Fig. 2a, FP exhibits significantly higher adsorption capacity towards $CO_2$ compared to Nafion, indicating the potential for improved gas transport within the catalyst layer. Furthermore, we compared the CO permeability of the two polymers, with FP exhibiting ~55 times higher permeability than Nafion (Fig. S3, Table S1). This finding further underscores the potential of FP to elevate the local CO concentration within the catalyst layer.

The $Cu_2O$ was synthesized according to a modified procedure [29]. As shown in the scanning electron microscopy (SEM) and transmission electron microscopy (TEM) images (Fig. 2b-c), the obtained $Cu_2O$ exhibits uniform cubic structure with an average particle size of 25 nm. Then a conventional catalyst layer preparation procedure was employed to fabricate the polymer/$Cu_2O$ composite on the gas diffusion layer (GDL). Typically, FP and Nafion were first mixed with $Cu_2O$ in their corresponding ink solutions, followed by sonication to afford a homogenous ink. The resulting ink was then spray-coated onto GDL to form the $Cu_2O$ catalyst layer. Thereafter, the FP/$Cu_2O$- and Nafion/-$Cu_2O$-based GDEs are abbreviated as FP/$Cu_2O$ and $Cu_2O$, respectively, for simplicity. Also, there is no Nafion used for preparing the FP/$Cu_2O$, as FP itself can act as catalyst binder. The as prepared FP/$Cu_2O$ also show larger contact angles than that of $Cu_2O$ (Fig. S4), indicating the desired hydrophobic properties of FP/$Cu_2O$.

Next, SEM and TEM were performed to study the morphology of the FP polymer modified $Cu_2O$. As shown in Fig. 2d-e, after warping with FP, the cubic structure of $Cu_2O$ is retained, and a thin polymer layer is clearly formed on the surface, with an average thickness of ~3.3 nm. Besides, the inverse FFT image (insert in Fig. 2e) reveals a (100) lattice with lattice spacing of 0.21 nm, which corresponds well with the intrinsic (200) facet spacing of $Cu_2O$ [34]. This suggest that the $Cu_2O$ surface modification with FP does not alter the morphological structure and crystallinity of the Cu catalyst. Furthermore, the X-ray powder diffraction (XRD) patterns (Fig. S5) of FP/$Cu_2O$ and $Cu_2O$ were found to be identical, with peak intensities and positions are consistent with those of cuprite (JCPDF NO. 05–0667). This further confirm that FP modification does not alter the crystal structure of the catalyst. Moreover, TEM-EDS (Energy-Dispersive X-ray spectroscopy) images revealed the even distribution of Cu, O and F elements on the $Cu_2O$ surface (Fig. 2g-i), indicating the homogenous modification of polymer on the catalyst surface.

The chemical state of $Cu_2O$ was examined by X-ray photoelectron spectroscopy (XPS) and X-ray absorption spectroscopy (XAS). As shown in Fig. 2j, the XPS of both $Cu_2O$ and FP/$Cu_2O$ display two peaks at 932.7 and 952.5 eV, corresponding to Cu $2p_{3/2}$ and Cu *2p1/2*, respectively. These binding energies are consistent with previously reported values for $Cu_2O$ [35]. In addition, the Cu Auger peak of FP/$Cu_2O$ shown in Fig. 2k exhibits the characteristic peak of $Cu_2O$, thereby confirming the surface oxidation state of Cu to be + 1. Besides, the existence of the FP polymer is confirmed by the F *1 s* peak in the XPS of FP/$Cu_2O$, agrees well with the EDX results (Fig. 2i and Fig. S6). Notably, the peaks corresponding to Cu *2p* and Cu *LMM* of FP/$Cu_2O$ are identical to those of the $Cu_2O$, suggesting that the FP modification does not alter the surface oxidation state of Cu. Moreover, Cu K-edge XAS for the two samples are also identical, further confirming that the chemical state of $Cu_2O$ catalyst is not altered by the polymer coating. Taken together, these results strongly demonstrate the successful coating of FP on the surface of $Cu_2O$ without altering the morphology or crystal phase of $Cu_2O$.

### 3.2. COR performances

To validate our strategy, the COR performance of FP/$Cu_2O$ was evaluated using a three-electrode flow cell (Fig. S1). Hereinafter, all potentials mentioned are referenced to the reversible hydrogen electrode (RHE), unless stated otherwise.

Fig. 3a-b exhibit the products distribution of COR base on FP/$Cu_2O$ and $Cu_2O$, respectively. Gaseous products including $H_2$, $CH_4$ and $C_2H_4$ were identified and quantified by gas chromatography spectroscopy. Liquid products including acetate, ethanol, and propanol were identified and quantified by the proton nuclear magnetic resonance ($^1$H NMR) spectroscopy (Fig. S7). In general, the two electrodes exhibited similar products distributions, suggesting similar reaction pathways involved (Table S2-S3). Encouragingly, FP/$Cu_2O$ exhibited significantly higher acetate Faradic efficiency ($FE_{acetate}$) compared to the $Cu_2O$ electrode, over an extended potential range. This enhanced acetate selectivity on FP/$Cu_2O$ is likely achieved on the expense of the selectivity towards other multi-carbon ($C_{2+}$) products, *i. e.*, $C_2H_4$, EtOH and PrOH (Fig. S8). Furthermore, we observed that the FE of acetate increase on both electrodes with increasing current density (Fig. 3**c**). As a result, the ratios of $FE_{oxygenates}/FE_{C2H4}$ and $FE_{acetate}/FE_{oxygenates}$ also increase as the increase of current density (Fig. S9). This increase in current density corresponds to an increase in cathodic potentials (Fig. S10), indicating that the ratios of $FE_{oxygenates}/FE_{C2H4}$ and $FE_{acetate}/FE_{oxygenates}$ increase alongside the increase of cathodic potentials, with FP/$Cu_2O$ exhibiting higher ratios compared to those of $Cu_2O$ (Fig. 3d-e). Similar potential dependent trends have been observed in a recent report, where these two ratios increased with the increased cathodic potential and CO partial pressure [27]. Hence, we tentatively attribute the enhanced $FE_{acetate}$ in FP/$Cu_2O$ to the higher cathodic potential and/or improved local CO concentration at the same current densities.

To explore the origin of the enhanced $FE_{acetate}$ of COR on FP/$Cu_2O$, we first examined the influence of cathodic potential, which is known to be able to steer the COR selectivity. As shown in Fig. S10, FP/$Cu_2O$ exhibit slightly higher cathodic potentials compared to $Cu_2O$ at low current densities until $-0.8$ A $cm^{-2}$. However, at higher current densities, FP/$Cu_2O$ demonstrates lower cathodic potentials for COR compared to $Cu_2O$, likely due to its robust hydrophobic nature

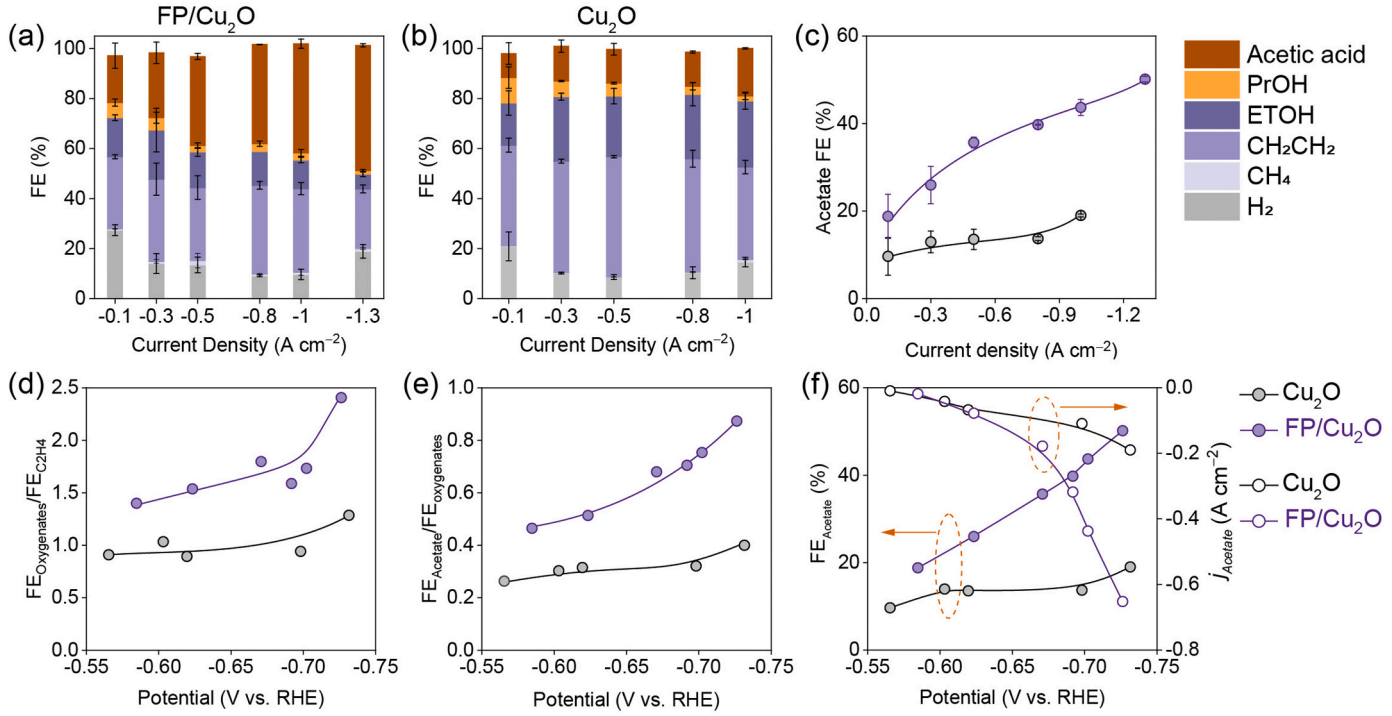


**Fig. 3.** Electrochemical COR on FP/$Cu_2O$. Faradic efficiencies (FEs) of the COR products on (a) FP/$Cu_2O$ and (b) $Cu_2O$; (c) comparison of acetate FEs at the same current density; FE ratio of (d) oxygenates/$C_2H_4$ and (e) acetate/oxygenates at the same potentials; (f) comparison of FE and partial current density of acetate on the two catalysts at the same potentials.

preventing the electrode flooding. This conclusion was made due to the following observations and considerations: (1) obvious increase in both $FE_{H2}$ and $j_{H2}$ was observed only on the $Cu_2O$ electrode rather than the FP/$Cu_2O$, as depicted in Fig. S11; (2) no evidence suggesting that FP/$Cu_2O$ is intrinsically different than $Cu_2O$ regarding the nature of the active-sties; (3) Cu is known as an inefficient catalyst for HER, especially under alkaline conditions[36], we anticipate that the overpotential may be increased when the electrode reaction shifts from COR and HER. Nevertheless, to determine whether the increased $FE_{acetate}$ on FP/$Cu_2O$, particularly at low current density region, is solely attributed to the slight differences in applied cathodic potentials, we compared the $FE_{acetate}$ and partial current density of acetate for both FP/$Cu_2O$ and $Cu_2O$ under identical cathodic potentials. As shown in Fig. 3f, intriguingly, FP/$Cu_2O$ exhibits higher FE and activity towards acetate compared to $Cu_2O$ at all applied cathodic potentials. Notably, the $FE_{acetate}$ on FP/$Cu_2O$ reached over 50% with a high partial current density of $-0.65$ A $cm^{-2}$, outperforming most reported Cu-based COR catalyst under ambient pressure (Fig. S12) [34,37–42]. In contrast, under the same conditions, $Cu_2O$ achieves a maximum acetate partial current density of only $-0.19$ A $cm^{-2}$ ($FE_{acetate} < 20\%$), approximately 3 times lower than that of FP/$Cu_2O$. Hence, it can be concluded that the applied cathodic potential is not the primary factor contributing to the increased $FE_{acetate}$. Instead, we hypothesize that the increased local CO concentration resulting from FP modification, is responsible for the improved selectivity and activity of COR towards acetate on FP/$Cu_2O$ under ambient pressure.

### 3.3. Influences of FP loading and CO partial pressure on COR performances

We anticipate that the local transportation CO is tied, possibly significantly, to the loading of FP. Hence, we sought to investigate the FP loading effect to confirm the aforementioned hypothesis and also to further optimize the selectivity/activity to acetate. During the catalyst ink preparation, we varied the loading of FP from 5 μL to 60 μL while keeping the catalyst loading constant. Under the same conditions, a FP loading of 20 μL in the catalyst ink was identified as the most optimized, as it resulted in the highest $FE_{acetate}$ (Fig. 4a, Fig. S13 and Table S4). We believe that the low loading of FP could not lead to a uniform polymer layer that fully cover the catalyst surface. This could result in insufficient gas diffusion, reduced hydrophobicity, and further contributing to the electrode flooding, especially at high current densities ($> -0.3$ A $cm^{-2}$, as shown in Fig. S14). In contrast, too high loading of FP will lead to very thick polymer layer on top of the catalyst surface, inhibiting mass transportation of both CO and water. In addition, the electronic conductivity of the catalyst layer will be compromised, leading to higher overpotentials and decreased COR performances (Fig. 3c and Fig. S14b). Electrochemical impedance spectroscopy (EIS) was employed to explore the influence of FP coating on proton/electron transfer. As show in Fig. S15, the solution resistance ($R_s$) for both FP/$Cu_2O$ (with optimal loading) and $Cu_2O$ are comparable, indicating that the coating of the FP polymer does not have a discernible impact on the electrode conductivity. It is also noted that FP/$Cu_2O$ electrode possesses a slightly higher electron transfer resistance ($R_{ct}$) compared to that of the $Cu_2O$ electrode, demonstrating a slightly slower reaction kinetics of FP/$Cu_2O$ compared to $Cu_2O$ under identical cathodic potentials. This aligns well with our experimental results, where, at the same current densities, FP/$Cu_2O$ exhibits higher overpotentials (Fig. S10). This is likely attributable to a shift in product selectivity from $C_2H_4$ to acetic acid. It is noted that an additional semicircle occurred for $Cu_2O$ at applied potentials from $-0.48$ V to $-0.58$ V. This semicircle was assigned to the diffusion-related charge transfer resistance ($R_p$) [43]. The relative value of $R_p$ to $R_{ct}$ ($R_p/R_{ct}$, Fig. S15c, right figure) increased with increasing applied cathodic potentials. We hypothesize that this emergent semicircle results from insufficient CO diffusion, impeding the adsorption kinetics of CO on the catalyst surface, which is especially noticeable at high current densities, where CO diffusion limitations become more pronounced. In conclusion, while the optimal FP coating does not notably impact catalyst conductivity, it does influence reaction kinetics. The FP promotes CO diffusion, reducing CO electro-adsorption resistance and

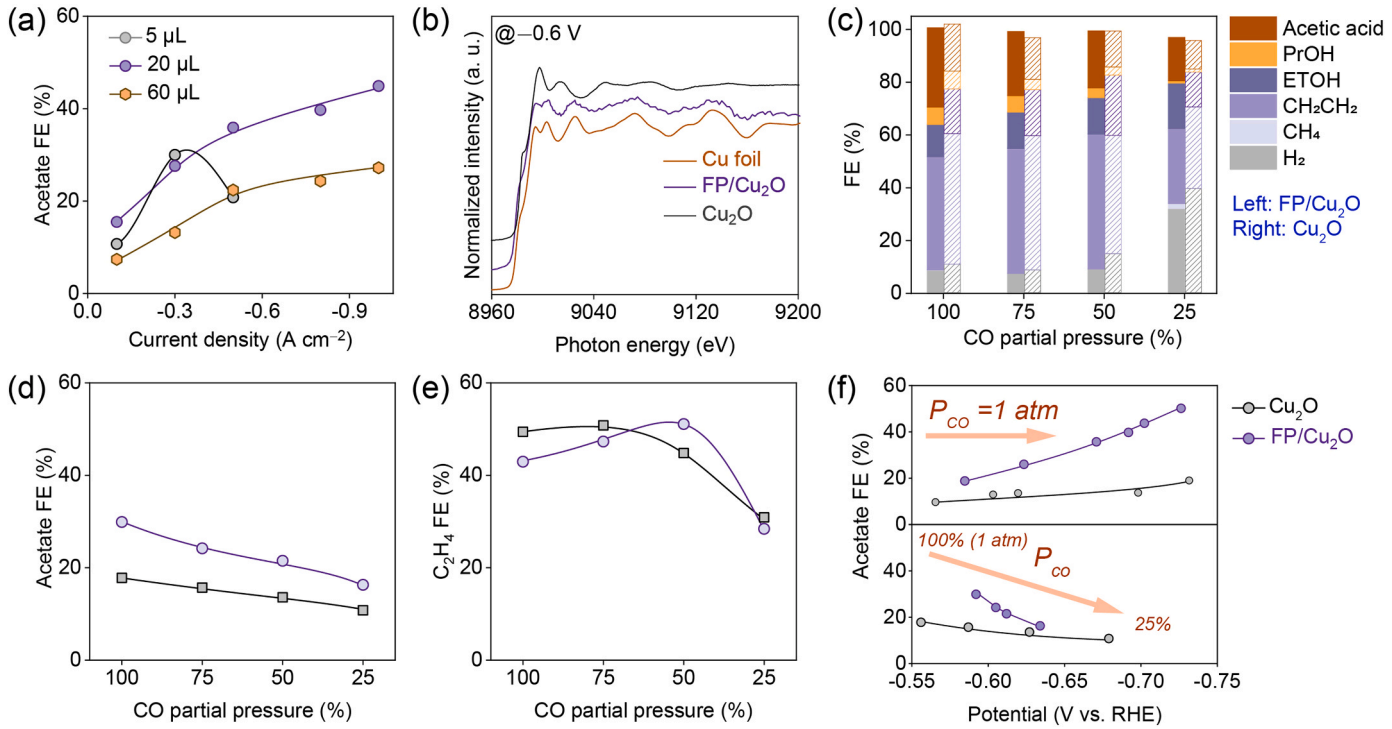


**Fig. 4.** (a) acetate selectivity with varied FP loadings, (b) in-situ X-ray absorption near-edge spectroscopy (XANES) spectra at the Cu K-edge; (c-e) CO partial pressure effect of (c) COR products distribution, (d) acetate selectivity, (e) $C_2H_4$ selectivity under varied CO partial pressures at current density of −0.3 A cm$^{-2}$; (f) comparison of acetate selectivity under atmospheric pressure and varied CO partial pressures, the upper one was tested under constant CO pressure, the below one was tested at varied CO partial pressure, decreased from 100% to 25%.

ultimately enhancing acetate selectivity.

Considering that Cu-based catalysts may undergo morphological and crystal phase changes and further influence the products selectivity/activity when interacting with surface ligands or polymers during electrocatalysis[38,44], it is crucial to conduct in-situ and post characterizations of FP-modified $Cu_2O$ to confirm whether such interactions exist and their influence on COR. Hence, we conducted the post-characterizations (*i.e.*, SEM, TEM, XRD and XPS) and in-situ XANES. As depicted in Fig. S16, the cubic structure of $Cu_2O$ collapsed in both the FP/$Cu_2O$ and $Cu_2O$ samples, indicating a structural change of $Cu_2O$ during the COR (Fig. S16a-e). Besides, the structural evolutions for both samples are similar. Additionally, the HRTEM images in Fig. S16c and f reveal the presence of rich facets/grain boundaries, and lattice defects due to the reconstruction of $Cu_2O$ during COR. Note, the $Cu_2O$ (111) facet appeared in both samples after electrolysis, attributed to the exposure of Cu to air after electrolysis for the TEM sample preparation, as observable in the inset images in Fig. S16c and f. As shown in Fig. S17a, XRD analysis revealed that both the FP/$Cu_2O$ and $Cu_2O$ were reduced to metallic Cu after COR, showing the peaks for the crystal planes of Cu (111), Cu (100), and Cu (220). The minor oxidized phase is likely caused by air exposure during sample preparation, which has also been supported by the HRTEM images (Fig. S16c and f). Similarly, we observed identical XPS of Cu *2p* (Fig. S17b) for both electrodes after COR. For Cu LMM Auger spectra, previous studies have identified two final-state terms, $^1$G and $^3$F, split from the L-S coupling. The $^1$G peaks are detected at 917.1 ($Cu^{2+}$), 915.8 ($Cu^{1+}$), and 918.0 eV ($Cu^0$) [45–47]. The $^3$F peak is only visible in the case of $Cu^0$ [44]. In the Fig. S17c, the presence of the $^1$G peak at 917.2 eV in both catalysts indicates the mono-valence state of Cu. Meanwhile, the distinct $^3$F peak confirms the existence of $Cu^0$. These results align with the above XRD results, which suggest that the catalysts were reduced to metallic Cu but experienced quickly surface oxidized upon exposed to air. Nevertheless, the Cu LMM Auger spectra further confirmed the similar chemical states of the two Cu catalysts. Besides, the presence of F 1 s peak suggest that the FP thin layer retains during COR (Fig. S17d). When extended the electrolysis time to 5 h, the F *1 s* spectrum remained observable, and the F content relative to Cu decreased from 15% to 10% after 5 h of electrolysis (Fig. S17e-f), suggesting the relative stability of the FP coating method. Furthermore, to accurately assess the chemical state of Cu during COR, in-situ XANES was conducted under the same COR conditions (*i.e.*, reactor, electrolytes, current density ranges, *etc.*). As shown in Fig. 4b, the adsorption edges of Cu in both samples are identical to that of Cu foil, indicating the formation of metallic Cu during COR. Additionally, similar double layer capacitances were estimated for both $Cu_2O$ and FP/$Cu_2O$ (Fig. S18), excluding the surface area effect on the COR selectivity [14,48,49]. Based on these comprehensive characterizations, it can be concluded that the observed difference in catalytic performance, especially the acetate selectivity/activity, are not attributed to variations in the morphology, chemical states and electrode surface area of FP/$Cu_2O$ and $Cu_2O$.

Previous reports have claimed that the acetate formation is also dependent on the alkalinity of the electrolyte [41,50]. To examine the influence of pH on acetate formation in our case, the KOH electrolyte concentration was varied within the range of 0.01–1 M, however, using $K_2SO_4$ to maintain the consistent cation concentration. As shown in Fig. S19, the products distribution of COR and required overpotentials (reference to standard hydrogen electrode, SHE) at −0.3 A cm$^{-2}$ show minor differences across different $OH^-$ concentrations. In addition, the FE for acetate and other $C_{2+}$ products also exhibit negligible dependence on pH, at least within the tested pH region (12–14) (Fig. S19b). Therefore, we believe pH is not a major factor that contributor to the enhanced acetate selectivity on FP/$Cu_2O$.

To validate our hypothesis regarding the promotion of CO diffusion induced by FP coating, we performed CO partial pressure ($P_{CO}$) dependent COR on both FP/$Cu_2O$ and $Cu_2O$ electrodes. As shown in Fig. 4c-d, a decreased $FE_{acatate}$ is observed on both electrodes with decrease in $P_{CO}$. Specifically, as the $P_{CO}$ decreased from 100% to 25%, the $FE_{acatate}$ on FP/$Cu_2O$ and $Cu_2O$ decreased from 29.9%, 17.8–16.3%, 10.8%,

respectively, at the current density of −0.3 A $cm^{-2}$. Conversely, $FE_{C2H4}$ on FP/$Cu_2O$ showed an inverse trend where it increased as the $P_{CO}$ decreased until a low $P_{CO}$ of 25% was applied (Table S5). This phenomenon has been reported elsewhere and has been explained as the lower CO coverage reducing the lateral interaction between *CO, thus stabilizing the ethylene-relevant intermediates [18]. Notably, the CO diffusion reached its limitation at an earlier stage (a $P_{CO}$ of 50%) in absence of FP (Fig. 4e), indicating that FP modification can effectively promote CO diffusion and result in higher local CO concentration, which is likely the origin of the enhanced selectivity towards acetate. The enhanced local CO concentration was also validated by the in situ attenuated total reflection surface-enhanced infrared absorption spectroscopy (ATR-SEIRAS), as shown in Fig. S20. FP/Cu exhibited a more pronounced peak intensity compared to $Cu_2O$, indicating a higher *CO coverage. Consequently, this enhanced *CO coverage likely promotes the production of acetate, aligning well with the conclusion from the partial pressure experiment.

Another noteworthy finding from the CO partial pressure dependent COR experiments is the increased overpotential observed as the $P_{CO}$ decreased (Fig. S21). Since acetate formation is also potential dependent, as observed in our data (Fig. 3a) and elsewhere [28,41], we thus analyzed the correlations between the $FE_{acetate}$ and overpotential at constant and different $P_{CO}$, respectively. As a result, we found that the $FE_{acetate}$ decreased with decreasing $P_{CO}$, regardless of the increased overpotentials on both $Cu_2O$ and FP/$Cu_2O$. In contrast, when $P_{CO}$ was kept constant, the $FE_{acetate}$ exhibited a positive correlation with overpotentials, as shown in Fig. 4f. Nevertheless, FP/$Cu_2O$ exhibited enhanced acetate formation compared to $Cu_2O$. Overall, we conclude that the increased $FE_{acetate}$ on FP/$Cu_2O$ is primarily attributed to the enhanced CO concentration rather than other parameters, *i. e.*, overpotentials, electrode surface area, and pH.

In summary, the elevated CO concentration within the catalyst layer originates from the high hydrophobicity and CO permeability of FP. The high CO permeability ensures sufficient diffusion of CO to the catalyst surface, while the hydrophobicity helps maintain the three-phase interface, especially at high current densities. This increased local CO concentration promotes stable selectivity and activity in producing acetate from COR at high electrolysis rates.

### 3.4. COR Stability and catalyst structural evolution

The stability of COR on FP/$Cu_2O$ was also examined under a constant

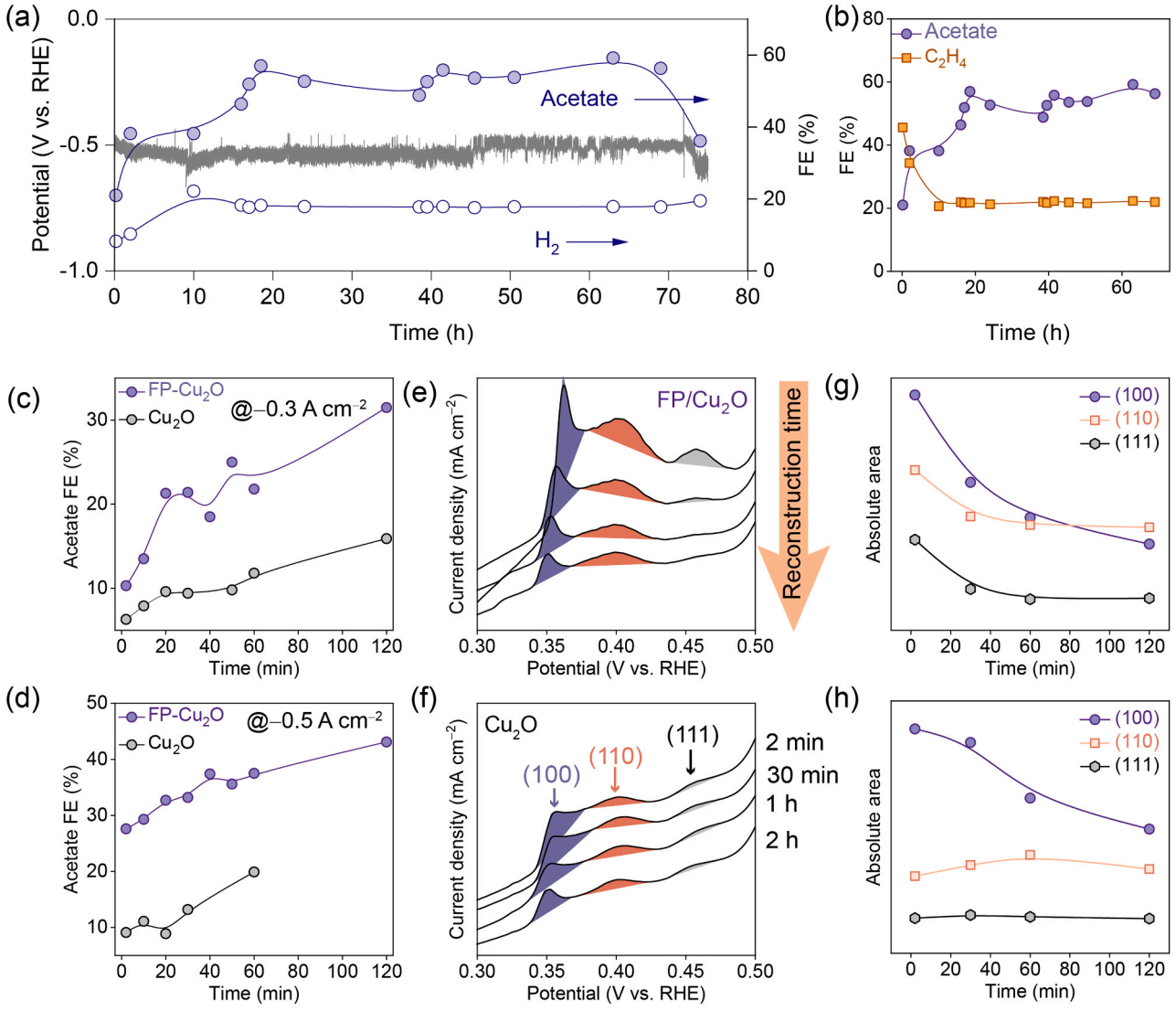


**Fig. 5.** (a) COR stability test with FP/$Cu_2O$ electrode at −0.3 A $cm^{-2}$ and (b) corresponding products FEs; $FE_{acetate}$ changes comparison of COR during 2-h test at current density of (c) −0.3 A $cm^{-2}$ and (d) −0.5 A $cm^{-2}$; (e-f) $OH_{ads}^{-}$ changes on (e) FP/$Cu_2O$ and (f) $Cu_2O$ at −0.3 A $cm^{-2}$; integrated $OH_{ads}^{-}$ area changes with time on (g) FP/$Cu_2O$ and (h) $Cu_2O$ at −0.3 A $cm^{-2}$.

current density of −0.3 A $cm^{-2}$ for 70 h in 1 M KOH (Fig. 5a). In contrast, the $Cu_2O$ electrode remained stable for only 27 h, after which a significant increase in $H_2$ selectivity was observed (Fig. S22). While with FP/$Cu_2O$, the relatively stable FE of $H_2$ throughout the stability test (Fig. 5a) indicates that the electrode did not experience severe flooding. This suggests that the FP coating, with its highly hydrophobic nature, can effectively improves the stability of the electrode. This enhancement is further corroborated by the post COR contact angle measurements (Fig. S23).

On the other hand, during the test, the acetate selectivity gradually increased and reached a peak of ~60% before the electrode failure. In contrast, the FE of $C_2H_4$ decreased within the first 20 h and then remained relatively stable for the remainder of the test (Fig. 5b and Table S6). Previous studies have suggested that the structural evolution of Cu catalyst during $CO_2R$ could lead to changes in the product distribution [51–53]. To examine the influence of this phenomenon, a chronopotentiometry test was conducted at both current densities of −0.3 and −0.5 A $cm^{-2}$ for a duration of 2 h on FP/$Cu_2O$. As depicted in Fig. 5c-d and Fig. S24, the FE of COR products exhibited time-dependent variations at both current densities. Particularly, the $FE_{acetate}$ displayed a monotonically increasing during the 2 h duration, while other products, *i.e.*, $C_2H_4$, EtOH and PrOH, experienced decrease in FE.

In-situ electrosorption of hydroxide ($OH_{ads}$) was employed to probe the surface structural change of the two electrodes (Fig. 5e-h) [41,54,55]. Qualitatively, both electrodes exhibited a prominent (100) $OH_{ads}$ feature, indicating a high surface density of (100) (Fig. 5e-f). However, the integral area of (100) $OH_{ads}$ gradually declined over time, suggesting the degradation of Cu (100) facet during the COR (Fig. 5g-h). Therefore, the observed decrease in $FE_{C2H4}$ during the COR test could be attribute to the deterioration of the Cu (100) facet, which are known to promote the formation of $C_2H_4$ [56,57]. In contrast, the integral areas of $OH_{ads}$ for the other two facets, Cu (110) and Cu (111) decreased rapidly until approximately 30 min, and remained relatively stable throughout the rest of the testing period. The significant decrease observed during initial 30 mins is likely attributed to the reduction of $Cu_2O$ to Cu or the degradation process of the structure (Fig. 5g-h). At this stage, the impact of these changes on COR products remains unclear, motivating further surface sensitive characterizations under real COR conditions to investigate the relationship between structural evolution and product selectivity. Of particular significance, the trends in product changes observed on FP/$Cu_2O$ and $Cu_2O$ electrodes are similar, indicating that the FP induced promotion effect is not resulted from the catalyst structural evolution during COR.

## 4. Conclusions

In summary, this work presents a strategy to enhance the local CO concentration under atmospheric pressure, leading to improved activity and selectivity towards acetate in COR. Specifically, the use of a full fluorinated polymer onto the surface of $Cu_2O$ catalyst, which facilitates the diffusion of CO and lead to high acetate FE of over 50% at a partial current density of − 0.65 A $cm^{-2}$. The influences from the changes in morphology, crystal phase, chemical states, active surface area have been excluded by post and in-situ characterizations/measurements. Additionally, CO partial pressure dependent COR further conformed the enhanced acetate formation is due to the increased local CO concentration resulting from the FP modification. Furthermore, the hydrophobic property of FP enables a stable operation of COR, resulting in stable electrolysis for 70 h at −0.3 A $cm^{-2}$. We believed that this strategy can be extended to other gas-involved electrocatalysis to steer the selectivity of products, especially those that are tied to the local gas concentrations.

## CRediT authorship contribution statement

**Junmei Chen**: Methodology, Conceptualization, formal analysis, investigation, data curation, writing-original draft. **Lei Chen, Jingyi Chen, Di Wang, Yilin Zhao, Lan Wen**: formal analysis, writing-review & editing. **ShiBo Xi**: formal analysis, Data curation, writing-review & editing. **Lei Wang**: Conceptualization, methodology, writing-review & editing, supervision, funding acquisition.

## Declaration of Competing Interest

The authors declare that they have no known competing financial interests or personal relationships that could have appeared to influence the work reported in this paper.

## Data Availability

Data will be made available on request.

## Acknowledgements

We acknowledge the National University of Singapore, Ministry of Education for their financial support, through the grants of A-0009176–02-00 and A-0009176–03-00, A*STAR (Agency for Science, Technology and Research) under its LCERFI program (Award No U2102d2002), Centre for Hydrogen Innovations at NUS (CHI-P2022-06). L. Wang would also like to acknowledge the support by National Research Foundation (NRF) Singapore, under NRF Fellowships (NRF-NRFF13-2021-0007). We thank Prof. Sui Zhang and Mr. Guangtai Zheng for support on the CO permeation measurements.

## Appendix A. Supporting information

Supplementary data associated with this article can be found in the online version at doi:10.1016/j.apcatb.2023.123551.

## References

[1] O.S. Bushuyev, P. De Luna, C.T. Dinh, L. Tao, G. Saur, J. van de Lagemaat, S. O. Kelley, E.H. Sargent, What should we make with $CO_2$ and how can we make it? Joule 2 (2018) 825–832.
[2] H. Shin, K.U. Hansen, F. Jiao, Techno-economic assessment of low-temperature carbon dioxide electrolysis, Nat. Sustain. 4 (2021) 911–919.
[3] F. Yu, G. Liu, J. Zhan, Y. Jia, Z. Feng, B. Shen, N.R. Shiju, L.-H. Zhang, Self-Driven Electron Enrichment of Ultrafine PdAu Nanoparticles for Electrochemical $CO_2$ Reduction: High Applicability of Work Function as an Activity Descriptor, Appl. Catal., B (2023), 122931.
[4] S. Kim, H. Shin, J.S. Kang, Electrochemical reduction of captured $CO_2$: a route toward the integrated carbon capture and utilization, Curr. Opin. Electrochem. (2023), 101321.
[5] C.-T. Dinh, T. Burdyny, M.G. Kibria, A. Seifitokaldani, C.M. Gabardo, F.P. García de Arquer, A. Kiani, J.P. Edwards, P. De Luna, O.S. Bushuyev, $CO_2$ electroreduction to ethylene via hydroxide-mediated copper catalysis at an abrupt interface, Science 360 (2018) 783–787.
[6] X. Liu, P. Schlexer, J. Xiao, Y. Ji, L. Wang, R.B. Sandberg, M. Tang, K.S. Brown, H. Peng, S. Ringe, pH effects on the electrochemical reduction of $CO_{(2)}$ towards $C_2$ products on stepped copper, Nat. Commun. 10 (2019) 32.
[7] W. Li, L. Li, Q. Xia, S. Hong, L. Wang, Z. Yao, T.-S. Wu, Y.-L. Soo, H. Zhang, T.W. B. Lo, Lowering C−C coupling barriers for efficient electrochemical $CO_2$ reduction to $C_2H_4$ by jointly engineering single Bi atoms and oxygen vacancies on CuO, Appl. Catal., B 318 (2022), 121823.
[8] J. Gu, S. Liu, W. Ni, W. Ren, S. Haussener, X. Hu, Modulating electric field distribution by alkali cations for $CO_2$ electroreduction in strongly acidic medium, Nat. Catal. 5 (2022) 268–276.
[9] D.W. Keith, G. Holmes, D.S. Angelo, K. Heidel, A process for capturing $CO_2$ from the atmosphere, Joule 2 (2018) 1573–1594.
[10] M. Ma, E.L. Clark, K.T. Therkildsen, S. Dalsgaard, I. Chorkendorff, B. Seger, Insights into the carbon balance for $CO_2$ electroreduction on Cu using gas diffusion electrode reactor designs, Energy Environ. Sci. 13 (2020) 977–985.
[11] J.E. Huang, F. Li, A. Ozden, A. Sedighian Rasouli, F.P. García de Arquer, S. Liu, S. Zhang, M. Luo, X. Wang, Y. Lum, $CO_2$ electrolysis to multicarbon products in strong acid, Science 372 (2021) 1074–1078.
[12] L. Wang, D.C. Higgins, Y. Ji, C.G. Morales-Guio, K. Chan, C. Hahn, T.F. Jaramillo, Selective reduction of CO to acetaldehyde with CuAg electrocatalysts, Proc. Natl. Acad. Sci. 117 (2020) 12572–12575.
[13] L. Wang, S.A. Nitopi, E. Bertheussen, M. Orazov, C.G. Morales-Guio, X. Liu, D. C. Higgins, K. Chan, J.K. Nørskov, C. Hahn, Electrochemical carbon monoxide reduction on polycrystalline copper: Effects of potential, pressure, and pH on

selectivity toward multicarbon and oxygenated products, ACS Catal. 8 (2018) 7445–7454.
[14] L. Wang, S. Nitopi, A.B. Wong, J.L. Snider, A.C. Nielander, C.G. Morales-Guio, M. Orazov, D.C. Higgins, C. Hahn, T.F. Jaramillo, Electrochemically converting carbon monoxide to liquid fuels by directing selectivity with electrode surface area, Nat. Catal. 2 (2019) 702–708.
[15] D.S. Ripatti, T.R. Veltman, M.W. Kanan, Carbon monoxide gas diffusion electrolysis that produces concentrated $C_2$ products with high single-pass conversion, Joule 3 (2019) 240–256.
[16] H. Rabiee, J.K. Heffernan, L. Ge, X. Zhang, P. Yan, E. Marcellin, S. Hu, Z. Zhu, H. Wang, Z. Yuan, Tuning flow-through cu-based hollow fiber gas-diffusion electrode for high-efficiency carbon monoxide (CO) electroreduction to $C_{2+}$ products, Appl. Catal., B 330 (2023), 122589.
[17] D. Kim, W. Choi, H.W. Lee, S.Y. Lee, Y. Choi, D.K. Lee, W. Kim, J. Na, U. Lee, Y. J. Hwang, Electrocatalytic reduction of low concentrations of $CO_2$ gas in a membrane electrode assembly electrolyzer, ACS Energy Lett. 6 (2021) 3488–3495.
[18] J. Li, Z. Wang, C. McCallum, Y. Xu, F. Li, Y. Wang, C.M. Gabardo, C.-T. Dinh, T.-T. Zhuang, L. Wang, Constraining CO coverage on copper promotes high-efficiency ethylene electroproduction, Nat. Catal. 2 (2019) 1124–1131.
[19] X. Chen, J. Chen, N.M. Alghoraibi, D.A. Henckel, R. Zhang, U.O. Nwabara, K. E. Madsen, P.J. Kenis, S.C. Zimmerman, A.A. Gewirth, Electrochemical $CO_2$-to-ethylene conversion on polyamine-incorporated Cu electrodes, Nat. Catal. 4 (2021) 20–27.
[20] R. Hegner, L.F. Rosa, F. Harnisch, Electrochemical $CO_2$ reduction to formate at indium electrodes with high efficiency and selectivity in pH neutral electrolytes, Appl. Catal., B 238 (2018) 546–556.
[21] W.J. Dong, J.W. Lim, J.Y. Park, C.J. Yoo, S. Baek, W.S. Cho, W. Kim, J.-L. Lee, Electric-field-driven electrochemical $CO_2$ reduction of sharpened Sn/Cu catalysts, Appl. Surf. Sci. 565 (2021), 150460.
[22] B. Yang, K. Liu, H. Li, C. Liu, J. Fu, H. Li, J.E. Huang, P. Ou, T. Alkayyali, C. Cai, Accelerating $CO_2$ electroreduction to multicarbon products via synergistic electric–thermal field on copper nanoneedles, J. Am. Chem. Soc. 144 (2022) 3039–3049.
[23] L.D. Chen, Cations play an essential role in $CO_2$ reduction, Nat. Catal. 4 (2021) 641–642.
[24] K. Guo, H. Lei, X. Li, Z. Zhang, Y. Wang, H. Guo, W. Zhang, R. Cao, Alkali metal cation effects on electrocatalytic $CO_2$ reduction with iron porphyrins, Chin. J. Catal. 42 (2021) 1439–1444.
[25] Z. Xing, L. Hu, D.S. Ripatti, X. Hu, X. Feng, Enhancing carbon dioxide gas-diffusion electrolysis by creating a hydrophobic catalyst microenvironment, Nat. Commun. 12 (2021) 136.
[26] L. Li, J. Chen, V.S.S. Mosali, Y. Liang, A.M. Bond, Q. Gu, J. Zhang, Hydrophobicity Graded Gas Diffusion Layer for Stable Electrochemical Reduction of $CO_2$, Angew. Chem. 134 (2022), e202208534.
[27] J. Hou, X. Chang, J. Li, B. Xu, Q. Lu, Correlating CO Coverage and CO Electroreduction on Cu via High-Pressure in Situ Spectroscopic and Reactivity Investigations, J. Am. Chem. Soc. 144 (2022) 22202–22211.
[28] R. Dorakhan, I. Grigioni, B.-H. Lee, P. Ou, J. Abed, C. O'Brien, A. Sedighian Rasouli, M. Plodinec, R.K. Miao, E. Shirzadi, A silver–copper oxide catalyst for acetate electrosynthesis from carbon monoxide, Nat. Synth. 2 (2023) 448–457.
[29] I.-C. Chang, P.-C. Chen, M.-C. Tsai, T.-T. Chen, M.-H. Yang, H.-T. Chiu, C.-Y. Lee, Large-scale synthesis of uniform $Cu_2O$ nanocubes with tunable sizes by in-situ nucleation, CrystEngComm 15 (2013) 2363–2366.
[30] P. Li, D. Paul, T.-S. Chung, High performance membranes based on ionic liquid polymers for $CO_2$ separation from the flue gas, Green. Chem. 14 (2012) 1052–1063.
[31] F.P. García de Arquer, C.-T. Dinh, A. Ozden, J. Wicks, C. McCallum, A.R. Kirmani, D.-H. Nam, C. Gabardo, A. Seifitokaldani, X. Wang, $CO_2$ electrolysis to multicarbon products at activities greater than 1 A $cm^{-2}$, Science 367 (2020) 661–666.
[32] J. Elliott, S. Hanna, A. Elliott, G. Cooley, The swelling behaviour of perfluorinated ionomer membranes in ethanol/water mixtures, Polymer 42 (2001) 2251–2253.
[33] H. Cavaye, R.J. Welbourn, J.G. Gluschke, P. Hughes, K.V. Nguyen, A.P. Micolich, P. Meredith, A.B. Mostert, Systematic in situ hydration neutron reflectometry study on Nafion thin films, Phys. Chem. Chem. Phys. 24 (2022) 28554–28563.
[34] P. Zhu, C. Xia, C.-Y. Liu, K. Jiang, G. Gao, X. Zhang, Y. Xia, Y. Lei, H.N. Alshareef, T.P. Senftle, Direct and continuous generation of pure acetic acid solutions via electrocatalytic carbon monoxide reduction, Proc. Natl. Acad. Sci. 118 (2021), e2010868118.
[35] P. Jiang, D. Prendergast, F. Borondics, S. Porsgaard, L. Giovanetti, E. Pach, J. Newberg, H. Bluhm, F. Besenbacher, M. Salmeron, Experimental and theoretical investigation of the electronic structure of $Cu_2O$ and CuO thin films on Cu (110) using x-ray photoelectron and absorption spectroscopy, J. Chem. Phys. 138 (2013), 024704.
[36] T. Zhao, J. Li, J. Liu, F. Liu, K. Xu, M. Yu, W. Xu, F. Cheng, Tailoring the Catalytic Microenvironment of Cu2O with SiO2 to Enhance C2+ Product Selectivity in $CO_2$ Electroreduction, ACS Catal. 13 (2023) 4444–4453.
[37] R. Dorakhan, I. Grigioni, B.-H. Lee, P. Ou, J. Abed, C. O'Brien, A. Sedighian Rasouli, M. Plodinec, R.K. Miao, E. Shirzadi, A silver–copper oxide catalyst for acetate electrosynthesis from carbon monoxide, Nat. Synth. (2023) 1–10.
[38] Y. Wang, J. Zhao, C. Cao, J. Ding, R. Wang, J. Zeng, J. Bao, B. Liu, Amino-Functionalized Cu for Efficient Electrochemical Reduction of CO to Acetate, ACS Catal. 13 (2023) 3532–3540.
[39] Y. Ji, Z. Chen, R. Wei, C. Yang, Y. Wang, J. Xu, H. Zhang, A. Guan, J. Chen, T.-K. Sham, Selective CO-to-acetate electroreduction via intermediate adsorption tuning on ordered Cu–Pd sites, Nat. Catal. 5 (2022) 251–258.
[40] X. Yan, M. Zhang, Y. Chen, Y. Wu, R. Wu, Q. Wan, C. Liu, T. Zheng, R. Feng, J. Zhang, Synergy of Cu/$C_3N_4$ Interface and Cu Nanoparticles Dual Catalytic Regions in Electrolysis of CO to Acetic Acid, Angew. Chem. Int. Ed. 62 (2023), e202301507.
[41] W. Luc, X. Fu, J. Shi, J.-J. Lv, M. Jouny, B.H. Ko, Y. Xu, Q. Tu, X. Hu, J. Wu, Two-dimensional copper nanosheets for electrochemical reduction of carbon monoxide to acetate, Nat. Catal. 2 (2019) 423–430.
[42] J. Jin, J. Wicks, Q. Min, J. Li, Y. Hu, J. Ma, Y. Wang, Z. Jiang, Y. Xu, R. Lu, Constrained C2 adsorbate orientation enables CO-to-acetate electroreduction, Nature (2023) 1–6.
[43] Z. Xing, X. Hu, X. Feng, Tuning the microenvironment in gas-diffusion electrodes enables high-rate $CO_2$ electrolysis to formate, ACS Energy Lett. 6 (2021) 1694–1702.
[44] H. Wu, J. Li, K. Qi, Y. Zhang, E. Petit, W. Wang, V. Flaud, N. Onofrio, B. Rebiere, L. Huang, Improved electrochemical conversion of $CO_2$ to multicarbon products by using molecular doping, Nat. Commun. 12 (2021) 7210.
[45] R.M. Arán-Ais, F. Scholten, S. Kunze, R. Rizo, B. Roldan, Cuenya, The role of in situ generated morphological motifs and $Cu_{(i)}$ species in $C_{2+}$ product selectivity during $CO_2$ pulsed electroreduction, Nat. Energy 5 (2020) 317–325.
[46] M. Favaro, H. Xiao, T. Cheng, W.A. Goddard III, J. Yano, E.J. Crumlin, Subsurface oxide plays a critical role in $CO_2$ activation by Cu (111) surfaces to form chemisorbed $CO_2$, the first step in reduction of $CO_2$, Proc. Natl. Acad. Sci. 114 (2017) 6706–6711.
[47] N. Pauly, S. Tougaard, F. Yubero, L.M.M. Auger, primary excitation spectra of copper, Surf. Sci. 630 (2014) 294–299.
[48] M. Goldman, A. Prajapati, E. Duoss, S. Baker, C. Hahn, Bridging Fundamental Science and Applied Science to Accelerate $CO_2$ Electrolyzer Scale up, Curr. Opin. Electrochem. (2023), 101248.
[49] D. Hursán, A.A. Samu, L. Janovák, K. Artyushkova, T. Asset, P. Atanassov, C. Janáky, Morphological attributes govern carbon dioxide reduction on N-doped carbon electrodes, Joule 3 (2019) 1719–1733.
[50] H.H. Heenen, H. Shin, G. Kastlunger, S. Overa, J.A. Gauthier, F. Jiao, K. Chan, The mechanism for acetate formation in electrochemical $CO_{(2)}$ reduction on Cu: selectivity with potential, pH, and nanostructuring, Energy Environ. Sci. 15 (2022) 3978–3990.
[51] J.A. Gauthier, J.H. Stenlid, F. Abild-Pedersen, M. Head-Gordon, A.T. Bell, The role of roughening to enhance selectivity to $C_{2+}$ products during $CO_2$ electroreduction on copper, ACS Energy Lett. 6 (2021) 3252–3260.
[52] S. Popović, M. Smiljanić, P. Jovanovič, J. Vavra, R. Buonsanti, N. Hodnik, Stability and degradation mechanisms of copper-based catalysts for electrochemical $CO_2$ reduction, Angew. Chem. 132 (2020) 14844–14854.
[53] J. Vavra, T.H. Shen, D. Stoian, V. Tileli, R. Buonsanti, Real-time monitoring reveals dissolution/redeposition mechanism in copper nanocatalysts during the initial stages of the $CO_2$ reduction reaction, Angew. Chem. 133 (2021) 1367–1374.
[54] D. Raciti, L. Cao, K.J. Livi, P.F. Rottmann, X. Tang, C. Li, Z. Hicks, K.H. Bowen, K. J. Hemker, T. Mueller, Low-overpotential electroreduction of carbon monoxide using copper nanowires, ACS Catal. 7 (2017) 4467–4472.
[55] J.M. Droog, B. Schlenter, Oxygen electrosorption on copper single crystal electrodes in sodium hydroxide solution, J. Electroanal. Chem. 112 (1980) 387–390.
[56] K.J.P. Schouten, E. Pérez Gallent, M.T. Koper, Structure sensitivity of the electrochemical reduction of carbon monoxide on copper single crystals, ACS Catal. 3 (2013) 1292–1295.
[57] G.L. De Gregorio, T. Burdyny, A. Loiudice, P. Iyengar, W.A. Smith, R. Buonsanti, Facet-dependent selectivity of Cu catalysts in electrochemical $CO_2$ reduction at commercially viable current densities, ACS Catal. 10 (2020) 4854–4862.